Astronomy & Astrophysics manuscript no. output
September 1, 2025

Messy disks and hungry stars: Do disk asymmetries shape protostellar growth?

A. Zuleta[1], A. Gupta[2], I. Cleeves[3], P. Curone[4],

[1] Institut de Ciències de l'Espai (ICE-CSIC), Campus UAB, Can Magrans S/N, E-08193 Cerdanyola del Vallès, Catalonia, Spain
e-mail: `azuleta@ice.csic.es`
[2] Department of Astronomy, University of Virginia, Charlottesville, VA 22904, USA
[3] Department of Chemistry, University of Virginia, 409 McCormick Road, Charlottesville, VA 22904, USA
[4] Departamento de Astronomía, Universidad de Chile, Camino El Observatorio 1515, Las Condes, Santiago, Chile

Received September 30, 20XX

ABSTRACT

Context. High-resolution ALMA observations have revealed that substructures such as rings, gaps, spirals, and asymmetries are common in protoplanetary disks. While rings and gaps are widespread across a broad range of stellar properties, asymmetries are rarer and their origin remains poorly understood. Previous studies have suggested possible links between asymmetries and stellar properties, but the results have been limited by sample size.

Aims. This work investigates the degree of asymmetry in protoplanetary disk substructure and its connection to stellar properties. The goal is to test whether asymmetries correlate with stellar mass, stellar accretion rate, and near-infrared (NIR) excess.

Methods. We analyzed the continuum emission directly in visibility space, modeling each disk as axisymmetric. The best-fit profile was subtracted from the data, and the resulting residuals were used to quantify the degree of asymmetry.

Results. We find positive correlations between Non-Axisymmetry Index (NAI) and stellar mass, stellar accretion rate, and near-infrared (NIR) excess. The parameter space shows two conspicuous gaps: there are no symmetric high-mass or high-accretion disks, and no asymmetric low-mass or low-accretion disks.

Conclusions. Asymmetries are more common in disks around higher-mass stars and strongly accreting systems.

Key words. Protoplanetary disks – Techniques: interferometric – Methods: data analysis

1. Introduction

High angular resolution observations of protoplanetary disks have revealed that these systems are far from smooth and host a wealth of substructure. Before the Atacama Large Millimeter/submillimeter Array (ALMA) era, evidence for disk substructure existed was inferred from spectral energy distribution (SED) modeling (Strom et al. 1989), images from the Hubble Space Telescope (Grady et al. 1999; Fukagawa et al. 2004), and pre-ALMA interferometers (Brown et al. 2008). These observational techniques provided important insights but lacked the resolution necessary to trace the dust emission at the spatial scales relevant for planet formation.

With ALMA, disk emission can now be resolved on scales of a few astronomical units, providing a transformative view of disk morphology (Andrews 2020). Resolved continuum observations have uncovered features suchs as concentric rings and gaps (ALMA Partnership et al. 2015; Andrews et al. 2016), spirals (Benisty et al. 2015; Huang et al. 2018), and arcs (Casassus et al. 2013; Isella et al. 2013), revealing that substructures are common across a wide range of stellar and disk properties. Among these morphologies, crescents and spirals are of particular interest. Arcs represent strong deviations from axisymmetry and are often interpreted as sites of efficient dust trapping (van der Marel et al. 2013), where pressure maxima prevent radial drift and allow solid particles to accumulate and facilitate planetesimal growth by enhancing the local dust-to-gas ratio (Birnstiel et al. 2013). Crescents are thought to form through Rossby wave instabilities, which generates long-lived vortices. They have been observed both as isolated structures (Casassus et al. 2013) and embedded within rings (Pérez et al. 2018). In contrast, spiral density waves can be triggered by companions (Ogilvie & Lubow 2002) or arise in sufficiently massive disks through gravitational instabilities triggered by perturbers at large scales (Kratter & Lodato 2016), although they do not accumulate dust.

Rings and gaps are the most frequently observed type of substructure, especially in millimeter continuum emission. Their occurrence appears to scale with the disk-to-star mass ratio, as disks with higher M_d/M_* are more likely to host multiple rings (Bae et al. 2023). These ringed disks are uniformly distributed across stellar properties and disk masses. Interestingly, most ringed systems show low near-infrared excesses (Benisty et al. 2023). Spirals, in contrast, are predominantly found around early-type stars, with sources with spirals show systematically higher near-infrared excesses than other morphologies (Garufi et al. 2018). Crescents are far less common, with only 13 reported cases. Although their occurrence rate reaches $\tilde{3}0\%$ for disks with $M_d/M_* > 0.05$, no clear dependence on stellar or disk properties has been identified (Bae et al. 2023).

The dependence of disk substructure on stellar and disk properties therefore varies with morphology, but the connection with asymmetries remains poorly constrained. A first attempt to link the degree of asymmetry to stellar properties was made by Curone et al. (2025), who reported tentative correlations with stellar mass, accretion rate, and NIR excess. However, their analysis was restricted by sample size and parameter coverage. In this paper, we build upon their work by expanding the sample size using ALMA archival data, allowing us to test correlations across a broader range of stellar and disk conditions with improved statistical significance. Sect. 2 describes the compilation of the source sample. Sect. 3 outlines the procedure used to model disk emission. Sect. 4 presents the metric to characterize asymmetries in the sample. In Sect. 5, we discuss the implications of our findings, and in Sect. 6, we outline potential future extensions of this work, including further exploitation of the ALMA archival data. Finally, the main conclusion are summarized in Sect. 5.

2. Sample and Data Selection

This work aims to investigate the degree of asymmetry in protoplanetary disks and its relation to stellar properties. To ensure a robust analysis, we restricted our study to sources that are sufficiently well resolved. Bae et al. (2023) compiled available ALMA observations of protoplanetary disks and showed that when the effective angular resolution $\theta_D/\theta_{\rm res} \geq 10$ (where θ_D is the angular diameter enclosing 90% of the continuum emission and $\theta_{\rm res}$ is the angular resolution of the observation), substructure are detected in 95% of the cases.

Following this this criterion, we selected sources with publicly available data products that meet the required level of resolution. However, since most of our sample comes from ALMA Large Programs, the sample is naturally biased toward the type of disks these programs were designed to observe. In particular, exoALMA was aimed at the largest and brightest disks in gas (Teague et al. 2025), while DSHARP focused on the largest and brightest nearby disks in dust continuum emission (Andrews et al. 2018). Additional sources were included when suitable Measurement Sets (MS) were available. A summary of the Program IDs and sources used for this work is given in Table 1.

2.1. exoALMA

The exoALMA large program targeted 15 very large, bright disks selected to the study of gas kinematics. By design, each target has a gas disk extending to ≥ 1″radius with moderate inclination (5 – 60°) and no signs of an envelope. The final sample spans spectral types from late F/G to M, but is strongly weighted toward more massive and luminous hosts with prominent dust substructure. Indeed, all but one target (PDS 66) exhibit deep continuum gaps or cavities. The targets are drawn from several star-forming regions at distances 90 – 310 pc.

Observations were conducted in ALMA Band 7 with a four spectral window (SPW) setup. Three SPWs were placed on single molecular lines: ^{12}CO (3−2), ^{13}CO (3−2), and CS (7−6), and the fourth SPW (1.875 GHz wide) was centered at 332 GHz for continuum. The line windows were recorded at the highest spectral resolution (15 kHz channels, yielding ≈ 30.5 kHz or ∼ 27 m/s effective resolution per channel). The continuum SPW was in frequency-division mode (488 kHz channels). The array was configured for ≈ 0.1″(14 – 20 au) resolution: a combination of C43-3 and C43-6 configurations (and additionally the Atacama Compact Array for the largest disks) was used, yielding a synthesized beam of ≈ 90 – 130 mas. The final calibrated datasets achieve 20 – 35μJy/beam noise in the continuum.

2.2. DSHARP

The Disk Substructures at High Angular Resolution Project (DSHARP) survey was designed to image a sample of 20 bright, nearby protoplanetary disks at a resolution down to ≈ 0.035″(5 au at ∼140 pc distance) to reveal small-scale substructures. Two key criteria shaped the target list: a beam resolution of a few AU to resolve narrow rings and gaps, and sensitivity to ≈ 10% continuum contrast out to tens of AU. The selection only considered Class II disks, while transition disks (with large central cavities) were excluded. The resulting DSHARP disks span spectral types from M to A, but on average host more massive/luminous stars than the typical disk population.

Observations were carried out in ALMA Band 6. Four dual-polarization spectral windows (SPWs) were used: three continuum SPWs (1.875 GHz each, centered near 232.6, 245.0, and 246.9 GHz, with 128 channels of 31.25 MHz) and one window covering the ^{12}CO (2–1) line at 230.538 GHz (938 MHz bandwidth, with 488 kHz channel spacing or 0.64 km/s channels). Each disk was observed in a "compact" C40-5 configuration (15 m-1.1 km baselines, ∼ 0.25″beam to recover large-scale emission) and in an "extended" C40-8 or C40-9 configuration (up to ∼ 12.1 km baselines, ∼ 0.035″beam). The combined data achieve a continuum rms of ∼ 10 – 25μJy/beam. The data reveal rich rings, gaps, and asymmetries in all targets.

2.3. Other sources

In addition to the exoALMA and DSHARP samples, we incorporated a small number of individual disks that satisfy our resolution requirements and provide complementary coverage of disk morphologies.

CS Cha was observed with ALMA in Band 7 with a correlator setup that included four spectral windows, with three dedicated to dust continuum emission, centered at 334.772, 336.600, and 347.471 GHz with a total bandwidth of 2 GHz, and one targeting line emission at 345.770 GHz. These data were originally presented by Kurtovic et al. (2022). Haro 6-13 was observed in Band 6, using a correlator configuration with four spectral windows centered at 224, 226, 240, and 242 GHz, each configured with 128 channels across a bandwidth of 2 GHz. The observations were first reported by Huang et al. (2025).

We also included three well-studied transition disks: AB Aur (Band 6), HD 142527 (Band 7), and IRS 48 (Band 7). For these systems, we relied on the data presented by Francis & van der Marel (2020), who analyzed a sample of transition disks with spatially resolved dust cavities. Together, these additional sources broaden the diversity of the sample by including disks with prominent cavities and complex morphologies beyond those covered by the large programs.

3. Methods

To isolate non-axisymmetric features in the disk emission, we modeled each source with an axisymmetric intensity profile `frank` (Jennings et al. 2020). This code employs a nonparametric approach to recover azimuthally averaged radial brightness profiles under the assumption of axisymmetry. The brightness profile is represented as a Fourier-Bessel series and transformed to the Fourier domain via a discrete Hankel transform, where it is fitted directly to the observed interferometric visibilities.

Working in the visibility space allows `frank` to fully exploit the sensitivity of the data and achieves sub-beam resolution compared to image-plane deconvolution methods such as CLEAN.

For each disk, the geometric parameters (inclination, position angle, and phase-center offsets) were fixed to the values listed in Table 1.

The modeling was performed in the LogNormal mode, which enforces positive fluxes and suppresses noise in regions of faint surface brightness. We tested the influence of the main hyperparameters in frank (α, $w_{\rm smooth}$, $R_{\rm max}$, N, and p_0). Given the sensitivity of the sample, variations within the recommended ranges produced negligible changes in the reconstructed profiles. For consistency, we adopted conservative values of the hyperparameters. Specifically, we set $\alpha = 1.3$ and $w_{\rm smooth} = 0.01$, where α defines the signal-to-noise threshold at which the model ceases to follow the visibilities and $w_{\rm smooth}$ damps spurious oscillations. The cutoff radius parameter, $R_{\rm max}$, beyond which frank assumes zero emission, was fixed to $1.5, R_{90}$. The number of grid points was set to $N = 400$, while the power spectrum regularization parameter, p_0, was kept at its standard value of 10^{-35} for logarithmic intensity fitting.

4. Results

4.1. Nonaxisymmetric Substructures

To identify non-asymmetric substructures, we followed the procedure outlined by Curone et al. (2025). Synthetic visibilities generated from the best-fitting `frank` model were subtracted from the observed visibilities, and reconstructed residual images from the resulting dataset using CASA task `tclean`.

The degree of non-axisymmetry was quantified using the non-axisymmetry index (NAI) defined by Curone et al. (2025). This metric provides a measure of the asymmetry level by comparing the residuals emission with the modeled emission. It is defined as:

$$\mathrm{NAI} = \frac{\sum_{i,j} \left| I_{\mathrm{res}\ i,j} \right|}{\sum_{i,j} \left| I_{\mathrm{mod}\ i,j} \right|} \quad \text{for SNR} \geq 5 \tag{1}$$

where $I_{\mathrm{res}\ i,j}$ and $I_{\mathrm{mod}\ i,j}$ denote the intensity at pixel $i,\ j$ of the CLEAN images corresponding to the `frank` residuals and the `frank` model, respectively. The calculation is restricted to pixels with a signal-to-noise ratio (SNR) $\geq$ 5 in the CLEAN image of the data, ensuring that the NAI only reflects statistically significant emission.

5. Discussion

5.1. Correlations

To assess the strength, direction, and significance of the correlations, we used the Kendall's τ correlation coefficient, which is robust against non-linear relationships and less sensitive to outliers. Fig. 1 shows the relations between stellar mass, mass accretion rate, and near-infrared excess as function of NAI. The NIR excess is defined as the flux above the stellar photosphere in the near-infrared, which traces the presence of hot dust in the innermost regions of the disk. For part of the sample, values were adopted from Garufi et al. (2018), for the remaining ones, the excess was derived following the same method: the observed fluxes from 2MASS and WISE photometry in the 1.2–4.5 μm range were dereddened and compared with a Phoenix stellar atmosphere model Hauschildt et al. (1999) with the appropriate effective temperature. The difference relative to the model photosphere was integrated and then normalized to the stellar flux to obtain the final NIR excess. Values for the stellar mass, mass accretion rate and NIR excess are reported in Table A.1.

For stellar mass, we find a weak positive correlation ($\tau = 0.20$, $p = 0.08$). Although not formally significant, this suggests that asymmetries tend to occur more frequently around higher-mass stars. A similar tendency was already noted by Curone et al. (2025), who probed sources up to $\sim$1.6 $M_\odot$ and found no significant correlation ($\tau = 0.10$, $p = 0.52$). Our sample extends up to $\sim$2.4 $M_\odot$, which may explain the stronger correlation.

For stellar mass accretion, we find $\tau = 0.27$ with $p = 0.02$, indicating a moderate, statistically significant correlation. Disks around stars with higher mass accretion rates are more likely to have asymmetries. This trend was not reported by Curone et al. (2025), likely because exoALMA lacks the high-accretors where asymmetries become more common. Our sample include sources with higher accretion rates above ($> 10^{-7} M_\odot \mathrm{yr}^{-1}$), beyond the upper range probed by exoALMA. When normalizing the accretion rate to stellar mass, the correlation weakens ($\tau = 0.15$, $p = 0.18$), differing from the stronger trend $\tau = 0.45$ with $p = 0.02$ reported by Curone et al. (2025).

The NIR excess shows a positive correlation with NAI ($\tau = 0.28$, $p = 0.02$), consistent with the idea that disks with stronger inner dust emission are more likely to exhibit asymmetries. Curone et al. (2025) reported stronger relation ($\tau = 0.48$, $p = 0.01$). Two notable outlier in our sample are RU Lup, which has a low NAI (0.05) despite a large NIR excess (42.3%), and IRS 48, which a strong asymmetry (NAI = 1.74) but only 2.6% NIR excess. These discrepancies may be linked to timescale differences. The NIR excess provides an instantaneous measure of the inner disk, whereas the development of substructures and asymmetries occurs on much longer timescales.

5.2. Extended emission

Following Curone et al. (2025), we characterized the millimeter continuum emission in the outer disk regions. For each source, we constructed azimuthally averaged radial intensity profiles from the deprojected continuum maps, considering radii between R_{90} and the point where the emission fell below 5σ. The profiles were then fitted with an exponentially tapered power law,

$$I\,(R) = I_0 \exp\left[-\frac{R}{\lambda_{\rm out}}\right], \tag{2}$$

where $\lambda_{\rm out}$ described the scale of the outer taper. To test wether the outer descent was sufficiently resolved, we also fitted A Gaussian profile centered on R_{90}:

$$I\,(R) = A \exp\left[-\frac{(x - R_{90})^2}{2\sigma_{\rm fit}^2}\right]. \tag{3}$$

We then computed $\sigma_{\rm fit}$ by $\sigma_{\rm beam}$, where $\sigma_{\rm beam}$ is the geometric mean of the synthesized beam axes. Values of $\lambda_{\rm out}$ and $\sigma_{\rm fit}/\sigma_{\rm beam}$ are reported in Table 4. We considered the descent in the outer profile to be reliably resolved when $\sigma_{\rm fit}/\sigma_{\rm beam} > 2$.

Fig. 2 shows the relation between R_{90} and $\lambda_{\rm out}$. Larger disks with larger dust radii tend to display shallower outer slopes, while more compact systems exhibit much steeper falloffs. A single system, Haro 6-13, deviates from the general distribution, but at present we cannot account for this special case.

Table 1. Dust Disk Geometrical parameters

Program ID (1)	Source (2)	i (deg) (3)	PA (deg) (4)	ΔR.A. (mas) (5)	ΔDecl. (mas) (6)	R_{90} (au) (7)	$\lambda_{\rm out}$ (au) (8)	$\sigma_{\rm fit}/\sigma_{\rm beam}$ (9)
2021.1.01123.L	AA Tau	$58.54^{+0.02}_{-0.02}$	$93.77^{+0.02}_{-0.03}$	$-5.46^{+0.11}_{-0.11}$	$4.83^{+0.07}_{-0.08}$	$139.4^{+1.2}_{-1.2}$	$22.6^{+1.0}_{-1.0}$	4.9
2021.1.01123.L	CQ Tau	$35.24^{+0.02}_{-0.02}$	$53.87^{+0.02}_{-0.02}$	$-8.71^{+0.05}_{-0.05}$	$0.99^{+0.04}_{-0.04}$	$73.1^{+0.6}_{-0.6}$	$11.9^{+0.4}_{-0.4}$	2.9
2021.1.01123.L	DM Tau	$35.97^{+0.05}_{-0.05}$	$155.60^{+0.08}_{-0.07}$	$-5.51^{+0.07}_{-0.07}$	$-6.59^{+0.09}_{-0.09}$	$201.9^{+1.2}_{-1.2}$	$70.3^{+9.7}_{-9.7}$	10.7
2021.1.01123.L	HD 135344B	$20.73^{+0.02}_{-0.02}$	$28.92^{+0.09}_{-0.06}$	$0.80^{+0.05}_{-0.05}$	$-3.21^{+0.05}_{-0.05}$	$90.2^{+1.2}_{-1.2}$	$6.8^{+0.1}_{-0.1}$	2.1
2021.1.01123.L	HD 143006	$18.69^{+0.09}_{-0.09}$	$7.53^{+0.35}_{-0.32}$	$8.27^{+0.14}_{-0.13}$	$26.42^{+0.16}_{-0.16}$	$79.9^{+0.1}_{-0.1}$	$6.5^{+0.2}_{-0.2}$	1.4
2021.1.01123.L	HD 34282	$59.09^{+0.01}_{-0.01}$	$117.15^{+0.01}_{-0.01}$	$13.00^{+0.07}_{-0.08}$	$15.49^{+0.06}_{-0.06}$	$239.4^{+2.8}_{-2.8}$	$52.3^{+0.8}_{-0.8}$	6.3
2021.1.01123.L	J1604	$8.72^{+0.09}_{-0.07}$	$123.24^{+0.07}_{-0.15}$	$-74.82^{+0.07}_{-0.07}$	$-16.67^{+0.06}_{-0.06}$	$112.4^{+0.5}_{-0.5}$	$13.0^{+0.3}_{-0.3}$	2.5
2021.1.01123.L	J1615	$47.10^{+0.01}_{-0.01}$	$146.14^{+0.02}_{-0.02}$	$-44.32^{+0.05}_{-0.04}$	$-5.88^{+0.04}_{-0.05}$	$169.6^{+2.1}_{-2.1}$	$48.5^{+1.3}_{-1.3}$	7.1
2021.1.01123.L	J1842	$39.22^{+0.03}_{-0.04}$	$26.35^{+0.06}_{-0.06}$	$-3.16^{+0.07}_{-0.07}$	$-30.69^{+0.07}_{-0.07}$	$85.2^{+1.1}_{-1.1}$	$16.4^{+0.6}_{-0.6}$	3.0
2021.1.01123.L	J1852	$32.50^{+0.03}_{-0.05}$	$117.61^{+0.03}_{-0.03}$	$-23.41^{+0.04}_{-0.04}$	$1.91^{+0.04}_{-0.04}$	$69.9^{+0.7}_{-0.7}$	$9.9^{+0.3}_{-0.3}$	2.1
2021.1.01123.L	LkCa 15	$50.59^{+0.01}_{-0.02}$	$61.57^{+0.01}_{-0.01}$	$-16.84^{+0.05}_{-0.05}$	$20.83^{+0.05}_{-0.05}$	$156.3^{+2.5}_{-2.5}$	$32.4^{+1.3}_{-1.3}$	6.6
2021.1.01123.L	MWC 758	$7.27^{+0.23}_{-0.17}$	$76.17^{+0.13}_{-0.10}$	$25.48^{+0.13}_{-0.13}$	$18.42^{+0.12}_{-0.12}$	$91.4^{+1.2}_{-1.2}$	$6.3^{+0.2}_{-0.2}$	1.5
2021.1.01123.L	PDS 66	$32.02^{+0.03}_{-0.03}$	$8.91^{+0.05}_{-0.05}$	$-3.59^{+0.02}_{-0.02}$	$6.68^{+0.03}_{-0.03}$	$46.9^{+0.2}_{-0.2}$	$6.1^{+0.2}_{-0.2}$	1.9
2021.1.01123.L	SY Cha	$51.65^{+0.03}_{-0.02}$	$165.77^{+0.04}_{-0.04}$	$-12.66^{+0.12}_{-0.13}$	$28.16^{+0.18}_{-0.18}$	$197.7^{+1.6}_{-1.6}$	$37.7^{+1.3}_{-1.3}$	4.8
2021.1.01123.L	V4046 Sgr	$33.36^{+0.01}_{-0.01}$	$76.02^{+0.02}_{-0.01}$	$-50.94^{+0.03}_{-0.02}$	$-45.18^{+0.02}_{-0.02}$	$60.9^{+0.4}_{-0.4}$	$10.9^{+0.6}_{-0.6}$	4.2
2016.1.00484.L	AS 209	$34.97^{+0.13}_{-0.13}$	$85.76^{+0.16}_{-0.16}$	$1.9^{+0.5}_{-0.5}$	$-2.5^{+0.5}_{-0.5}$	$139^{+1.0}_{-1.0}$	$16.7^{+1.4}_{-1.4}$	3.1
2016.1.00484.L	DoAr 25	$67.4^{+0.2}_{-0.2}$	$110.6^{+0.2}_{-0.2}$	$38^{+2.0}_{-2.0}$	$-494^{+2.0}_{-2.0}$	$165^{+1.0}_{-1.0}$	$25.2^{+0.3}_{-0.3}$	4.3
2016.1.00484.L	DoAr 33	$41.8^{+0.8}_{-0.8}$	$81.1^{+1.2}_{-1.2}$	$1.5^{+0.8}_{-0.8}$	$0.6^{+0.6}_{-0.6}$	$27^{+1.0}_{-1.0}$	$3.1^{+0.3}_{-0.3}$	0.6
2016.1.00484.L	Elias 20	$49.0^{+1.0}_{-1.0}$	$153.2^{+1.3}_{-1.3}$	$-54.5^{+1.5}_{-1.5}$	$-491.0^{+1.3}_{-1.3}$	$64^{+1.0}_{-1.0}$	$12.1^{+0.3}_{-0.3}$	2.8
2016.1.00484.L	Elias 24	$29.0^{+0.3}_{-0.3}$	$45.7^{+0.7}_{-0.7}$	$110.8^{+0.8}_{-0.8}$	$-386.8^{+0.9}_{-0.9}$	$136^{+1.0}_{-1.0}$	$13.0^{+0.4}_{-0.4}$	2.3
2016.1.00484.L	Elias 27	$56.2^{+0.8}_{-0.8}$	$118.8^{+0.7}_{-0.7}$	$-5^{+5.0}_{-5.0}$	$-8^{+3.0}_{-3.0}$	$254^{+1.0}_{-1.0}$	$46.5^{+1.1}_{-1.1}$	6.7
2016.1.00484.L	GW Lup	$38.7^{+0.3}_{-0.3}$	$37.6^{+0.5}_{-0.5}$	$-2.4^{+1.1}_{-1.1}$	$-0.9^{+1.2}_{-1.2}$	$105^{+1.0}_{-1.0}$	$17.0^{+0.5}_{-0.5}$	1.5
2016.1.00484.L	HD 142666	$62.22^{+0.14}_{-0.14}$	$166.11^{+0.15}_{-0.15}$	$9.47^{+0.9}_{-0.9}$	$15.5^{+1.6}_{-1.6}$	$59^{+1.0}_{-1.0}$	$7.1^{+0.2}_{-0.2}$	1.7
2016.1.00484.L	HD 163296	$46.7^{+0.1}_{-0.1}$	$133.33^{+0.15}_{-0.15}$	$-2.8^{+0.7}_{-0.7}$	$7.7^{+0.7}_{-0.7}$	$169^{+1.0}_{-1.0}$	$57.7^{+5.3}_{-5.3}$	9.1
2016.1.00484.L	IM Lup	$47.5^{+0.3}_{-0.3}$	$144.5^{+0.5}_{-0.5}$	$-1.5^{+2.0}_{-2.0}$	$1.0^{+2.0}_{-2.0}$	$264^{+1.0}_{-1.0}$	$39.9^{+1.3}_{-1.3}$	4.0
2016.1.00484.L	MY Lup	$73.2^{+0.1}_{-0.1}$	$58.8^{+0.1}_{-0.1}$	$-77.9^{+0.8}_{-0.8}$	$62.9^{+0.6}_{-0.6}$	$87^{+1.0}_{-1.0}$	$12.2^{+0.3}_{-0.3}$	1.7
2016.1.00484.L	RU Lup	$18.8^{+1.6}_{-1.6}$	$121^{+5.0}_{-5.0}$	$-17.1^{+0.8}_{-0.8}$	$88.1^{+0.8}_{-0.8}$	$64^{+1.0}_{-1.0}$	$9.6^{+0.4}_{-0.4}$	2.2
2016.1.00484.L	SR4	$22.0^{+2.0}_{-2.0}$	$18^{+5.0}_{-5.0}$	$-56.4^{+1.2}_{-1.2}$	$-507.4^{+1.3}_{-1.3}$	$31+1.0_{-1.0}$	$2.5^{+0.2}_{-0.2}$	0.5
2016.1.00484.L	Sz 114	$21.3^{+1.3}_{-1.3}$	$165^{+4.0}_{-4.0}$	$-1.0^{+2.0}_{-2.0}$	$4.0^{+2.0}_{-2.0}$	$58^{+1.0}_{-1.0}$	$7.3^{+0.3}_{-0.3}$	0.8
2016.1.00484.L	Sz 129	$34.1^{+1.3}_{-1.3}$	$151^{+2.0}_{-2.0}$	$5.4^{+1.9}_{-1.9}$	$3.0^{+1.7}_{-1.7}$	$76^{+1.0}_{-1.0}$	$8.7^{+0.5}_{-0.5}$	1.4
2016.1.00484.L	WaOph 6	$47.3^{+0.7}_{-0.7}$	$174.2^{+0.8}_{-0.8}$	$-244^{+3.0}_{-3.0}$	$-361^{+3.0}_{-3.0}$	$103^{+1.0}_{-1.0}$	$19.9^{+1.1}_{-1.1}$	3.5
2016.1.00484.L	WSB52	$54.4^{+0.3}_{-0.3}$	$138.4^{+0.3}_{-0.3}$	$-119.5^{+0.4}_{-0.4}$	$-432.8^{+0.4}_{-0.4}$	$32^{+1.0}_{-1.0}$	$3.3^{+0.2}_{-0.2}$	0.8
2017.1.00969.S	CS Cha	$17.78^{+0.01}_{-0.05}$	82.6	$13.17^{+0.04}_{-0.06}$	$2.28^{+0.03}_{-0.08}$	$57^{+1.0}_{-1.0}$	$5.3^{+0.1}_{-0.1}$	0.8
2022.1.01365.S	Haro 6-13	$39.47^{+0.09}_{-0.09}$	$154.09^{+0.14}_{-0.14}$	$3.61^{+0.06}_{-0.06}$	$0.81^{+0.08}_{-0.08}$	$39^{+1.0}_{-1.0}$	$33.3^{+3.2}_{-3.2}$	5.0
2012.1.00303.S	AB Aur	23.0	50.0	-80	70	$231^{+1.0}_{-1.0}$	$26.7^{+0.1}_{-0.1}$	0.7
2012.1.00631.S	HD 142527	27.0	-20.0	24.2	0.3	$232^{+1.0}_{-1.0}$	$28.7^{+2.6}_{-2.6}$	2.4
2013.1.00100.S	IRS 48	50.0	100.0	-20.5	-18.6	$91^{+1.0}_{-1.0}$	$8.6^{+0.2}_{-0.2}$	0.5

Notes. Columns are defined as follows: (1) ALMA Program ID, (2) target name, (3) disk inclination, (4) disk PA. (5-6) offsets in R.A. and decl. between the disk center and the phase center, (7) radius containing 90% of the flux, (8) scale length of the outer disk taper $\lambda_{\rm out}$ from the exponential model $I(R) = I_0 \exp\left[R^2/\lambda_{\rm out}\right]$, and (9): ratio between the σfit from the Gaussian model $I(R) = A \exp\left[(x - R_{90})^2/2\sigma_{\rm fit}^2\right]$ and the $\sigma_{\rm beam}$ obtained by averaging the major and minor axis σ values of the synthesized beam. Values for the sources in exoALMA (2021.1.01123.L) were obtained from Curone et al. (2025). For projects not in exoALMA, we computed R_{90}, $\lambda_{\rm out}$, and $\sigma_{\rm fit}/\sigma_{\rm beam}$. For sources in DSHARP (2016.1.00484.L), geometrical parameters were obtained from Huang et al. (2018) except for the offset of HD 142666, for which we performed a Gaussian fitting. For CS cha, we obtained the values from Kurtovic et al. (2022). For Haro 6-13, we obtained the values from Huang et al. (2025). For AB Aur, HD 142527, and IRS 48, we got the parameters from Francis & van der Marel (2020), no uncertainties were associated with the source geometry.

5.3. Two populations

In Fig. 1, the distributions of stellar mass and accretion rate versus NAI, reveal two gaps in the parameter space. There are no symmetric massive disks, and no asymmetric low-mass or weakly accreting stars. These empty regions suggest that asymmetries are not randomly distributed but instead may reflect two distinct regimes.

We explored the hypothesis that the disks in our sample may be divided into two populations. The first corresponds to T Tauri stars (K–M types), which host lower-mass stars and disks, and (2) Herbig Ae/Be stars (early-type), which are more massive and luminous. To test this, we performed two-sample Kolmogorov–Smirnov (KS) tests on the NAI and NIR excess distributions. The cumulative distribution functions (CDFs), shown in Fig. 3, confirm statistically significant differences between

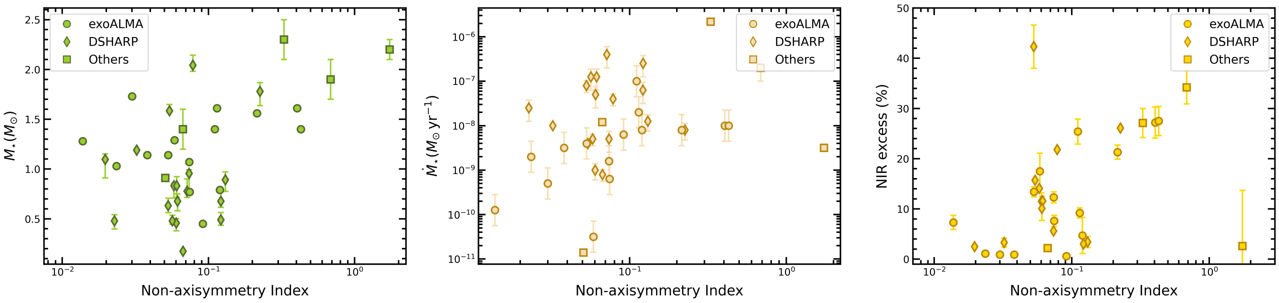

Fig. 1. Stellar properties against NAI. From left to right: stellar mass (M_*), mass accretion rate ($\dot{M}_{\rm acc}$), and Near-Infrared (NIR) excess. Data points are marked by their belonging to different observational programs (see Sec. 2). Error bars are shown for data points when this information was available.

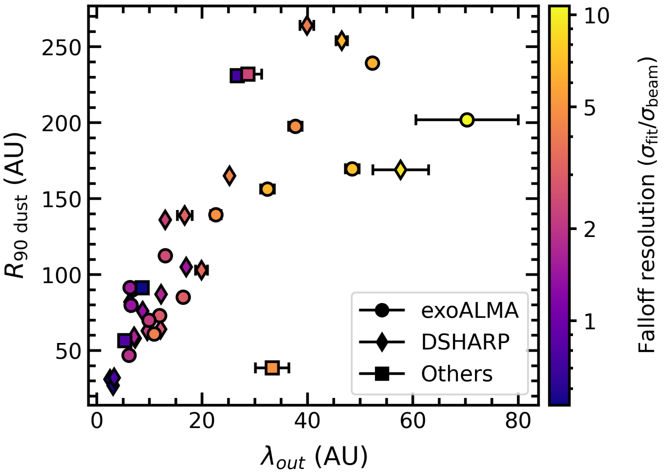

Fig. 2. Radius enclosing 90% of the continuum emission ($R_{90,\ \rm dust}$) as a function of $\lambda_{\rm out}$. The color scale represents the number of beams across the outer disk falloff, shown as $\sigma_{\rm fit}/\sigma_{\rm beam}$ on a logarithmic scale.

the two populations (NAI: $p = 1.39 \times 10^{-2}$; NIR excess: $p = 3.32 \times 10^{-2}$).

A possible explanation for the absence of symmetric massive disks is late-time gas infall, where ambient material is gravitationally captured through Bondi–Hoyle–Lyttleton (BHL) accretion. This process has been proposed as a mechanism sustaining stellar accretion in young stars (Padoan et al. 2005). Simulations show that infall can generate spirals and arcs (Kuffmeier et al. 2020) and trigger the Rossby wave instability that produces vortices (Bae et al. 2015; Kuznetsova et al. 2022). Estimates suggest that 20–70% of the final disk mass may be acquired through late infall (Winter et al. 2024). Observationally, Garufi et al. (2024) found that 16 of 43 disk-hosting stars show evidence of interaction with the surrounding ISM, supporting the idea that environment plays a critical role.

Conversely, smooth symmetric disks are most common in low-mass systems. By combining measurements of $R_{\rm dust}$ from resolved millimeter interferometric images with mid-infrared molecular spectra, Banzatti et al. (2020) reported an anticorrelation between the luminosity of H_2O luminosity and$R_{\rm dust}$. If Rdust is primarily determined by pebble drift, and molecular luminosities trace the elemental mass budget of the inner disk, this implie that icy pebbles drift inward, sublimate, and enrich the inner disk. The efficiency of this drift depends on disk structure: it is higher in smooth disks where radial pressure traps are absent, and suppressed in disks with substructures when pressure traps are present. Consequently, low-mass disks, which tend to be less structured would not be capable of having asymmetries.

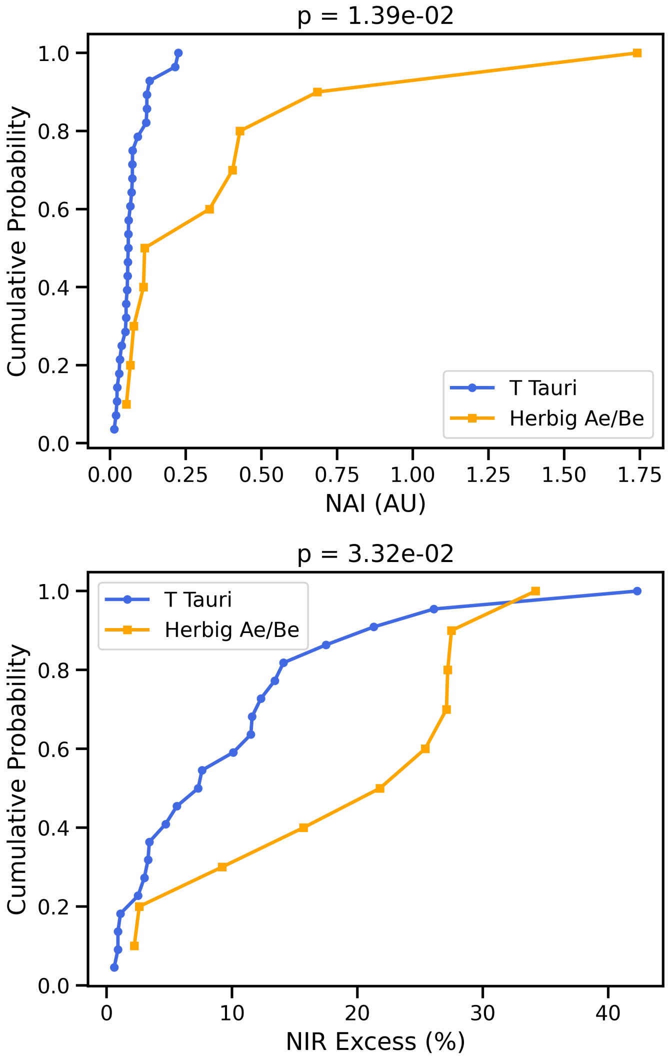

Fig. 3. Cumulative distribution functions (CDFs) for the (left) Non-axisymmetry Index (NAI) and (right) Near-Infrared (NIR) excess, comparing the populations of T Tauri stars (n=28) and Herbig Ae/Be stars (n=10). The results of two-sample Kolmogorov-Smirnov tests indicate a statistically significant difference between the two stellar types for both parameters (NAI: p = 1.39×10^{-2}, and NIR excess: p = 3.32×10^{-2})

6. Future Work

The initial study was focused on a biased subset of disks bright and large disk, but the analysis here can be extended to a broader population. Our selection was determined by having a effective angular resolution satisfies $\theta_D/\theta_{\rm res} \geq 10$ as criterion (see Sec. 2). To build a list of potential sources, we combined the ALMA archive with the catalog of young stars with near-infrared and/or millimeter data compiled by Bae et al. (2023), which covers the main nearby star-forming regions of Taurus, Ophiuchus, Upper Scorpius, Lupus, and Chamaeleon I. From this starting point, we queried the ALMA archive to identify additional suitable observations.

In practice, we selected observations meeting several conditions. Observations had to be in Band 6 or Band 7, with maximum recoverable scales larger than the disk size to ensure sensitivity to all emission scales. Only disks resolved with at least 10 synthesized beams across their diameter were kept. Assuming a Gaussian intensity profile, we used the integrated fluxes reported by Bae et al. (2023) to estimate radial intensity profiles and compute the signal-to-noise ratio at the radius enclosing 90% of the continuum emission (R_{90}). Disks with a SNR at R_{90} below the minimum measured in DSHARP were discarded. After applying these criteria, we identified 30 potential new sources that could be incorporated into the sample.

7. Conclusions

This work investigated the degree of asymmetry in protoplanetary disks and its connection to stellar properties. To ensure a robust analysis, we constructed a sample by combining ALMA archival data from exoALMA, DSHARP, and geometrically characterized sources. The final sample consisted of 37 well-resolved disks in nearby star-forming regions, allowing us to explore asymmetry trends in detail.

- We find evidence for correlations between stellar properties and disk asymmetry. Asymmetries are more frequent in disks around higher-mass stars and in systems with elevated stellar accretion rates. The near-infrared excess also correlates with asymmetry, suggesting a link between inner disk dust content and large-scale morphology.

- Two regions of parameter space remain unpopulated: there are no symmetric massive disks or high accretors, and no strongly asymmetric low-mass disks or low accretors. We interpret this difference as the presence of two distinct populations.

- The observed trends may be explained by physical processes that act differently across the stellar mass spectrum. In low-mass systems, efficient pebble drift and lack of substructure could deplete the outer disk, whereas in massive disks or high-accretion systems, late gas infall may continuously replenish material and drive substructure formation.

Future work should aim to expand the sample size, particularly toward both ends of the stellar mass range. A larger and more uniform dataset will be essential to test the generality of the trends identified here.

Acknowledgements. This work originated from a project of the Summer Program in Astrophysics 2025 held at the University of Virginia, and funded by the Center for Global Inquiry and Innovation, the National Science Foundation (Grant 2452494), the National Radio Astronomy Observatory (NRAO), the Kavli Foundation and the Heising-Simons Foundation.

References

ALMA Partnership, Brogan, C. L., Pérez, L. M., et al. 2015, ApJ, 808, L3
Andrews, S. M. 2020, ARA&A, 58, 483
Andrews, S. M., Huang, J., Pérez, L. M., et al. 2018, ApJ, 869, L41
Andrews, S. M., Wilner, D. J., Zhu, Z., et al. 2016, ApJ, 820, L40
Bae, J., Hartmann, L., & Zhu, Z. 2015, ApJ, 805, 15
Bae, J., Isella, A., Zhu, Z., et al. 2023, in Astronomical Society of the Pacific Conference Series, Vol. 534, Protostars and Planets VII, ed. S. Inutsuka, Y. Aikawa, T. Muto, K. Tomida, & M. Tamura, 423
Banzatti, A., Pascucci, I., Bosman, A. D., et al. 2020, ApJ, 903, 124
Benisty, M., Dominik, C., Follette, K., et al. 2023, in Astronomical Society of the Pacific Conference Series, Vol. 534, Protostars and Planets VII, ed. S. Inutsuka, Y. Aikawa, T. Muto, K. Tomida, & M. Tamura, 605
Benisty, M., Juhasz, A., Boccaletti, A., et al. 2015, A&A, 578, L6
Birnstiel, T., Dullemond, C. P., & Pinilla, P. 2013, A&A, 550, L8
Brown, J. M., Blake, G. A., Qi, C., Dullemond, C. P., & Wilner, D. J. 2008, ApJ, 675, L109
Casassus, S., van der Plas, G. M., Perez, S., et al. 2013, Nature, 493, 191
Costigan, G., Vink, J. S., Scholz, A., Ray, T., & Testi, L. 2014, MNRAS, 440, 3444
Curone, P., Facchini, S., Andrews, S. M., et al. 2025, ApJ, 984, L9
Espaillat, C., Calvet, N., D'Alessio, P., et al. 2007, ApJ, 664, L111
Follette, K. B., Grady, C. A., Swearingen, J. R., et al. 2015, ApJ, 798, 132
Francis, L. & van der Marel, N. 2020, ApJ, 892, 111
Fukagawa, M., Hayashi, M., Tamura, M., et al. 2004, ApJ, 605, L53
Garufi, A., Benisty, M., Pinilla, P., et al. 2018, A&A, 620, A94
Garufi, A., Ginski, C., van Holstein, R. G., et al. 2024, A&A, 685, A53
Grady, C. A., Woodgate, B., Bruhweiler, F. C., et al. 1999, ApJ, 523, L151
Hauschildt, P. H., Allard, F., & Baron, E. 1999, ApJ, 512, 377
Huang, J., Aizawa, M., Bae, J., et al. 2025, ApJ, 988, 106
Huang, J., Andrews, S. M., Dullemond, C. P., et al. 2018, ApJ, 869, L42
Isella, A., Pérez, L. M., Carpenter, J. M., et al. 2013, ApJ, 775, 30
Jennings, J., Booth, R. A., Tazzari, M., Rosotti, G. P., & Clarke, C. J. 2020, MNRAS, 495, 3209
Kratter, K. & Lodato, G. 2016, ARA&A, 54, 271
Kuffmeier, M., Goicovic, F. G., & Dullemond, C. P. 2020, A&A, 633, A3
Kurtovic, N. T., Pinilla, P., Penzlin, A. B. T., et al. 2022, A&A, 664, A151
Kuznetsova, A., Bae, J., Hartmann, L., & Mac Low, M.-M. 2022, ApJ, 928, 92
Lin, C.-L., Ip, W.-H., Hsiao, Y., et al. 2023, AJ, 166, 82
Long, F., Herczeg, G. J., Harsono, D., et al. 2019, ApJ, 882, 49
Manara, C. F., Ansdell, M., Rosotti, G. P., et al. 2023, in Astronomical Society of the Pacific Conference Series, Vol. 534, Protostars and Planets VII, ed. S. Inutsuka, Y. Aikawa, T. Muto, K. Tomida, & M. Tamura, 539
Mendigutía, I., Fairlamb, J., Montesinos, B., et al. 2014, ApJ, 790, 21
Ogilvie, G. I. & Lubow, S. H. 2002, MNRAS, 330, 950
Padoan, P., Kritsuk, A., Norman, M. L., & Nordlund, Å. 2005, ApJ, 622, L61
Parker, R., Ward-Thompson, D., & Kirk, J. 2022, MNRAS, 511, 2453
Pérez, L. M., Benisty, M., Andrews, S. M., et al. 2018, ApJ, 869, L50
Strom, K. M., Strom, S. E., Edwards, S., Cabrit, S., & Skrutskie, M. F. 1989, AJ, 97, 1451
Teague, R., Benisty, M., Facchini, S., et al. 2025, ApJ, 984, L6
van der Marel, N., van Dishoeck, E. F., Bruderer, S., et al. 2013, Science, 340, 1199
Winter, A. J., Benisty, M., & Andrews, S. M. 2024, ApJ, 972, L9

Appendix A: Mass, accretion rate, and NIR excess

Table A.1. Stellar properties for our sample

Source (1)	$\log_{10} M_*$ $(M_\odot)$ (2)	$\log_{10} \dot{M}$ $(M_\odot \mathrm{yr}^{-1})$ (3)	NIR excess (%) (4)	References (5)
AS 209	$-0.08^{+0.11}_{-0.14}$	$-7.3^{+0.5}_{-0.5}$	$10.1^{+2.4}_{-2.4}$	(Huang et al. 2018; Garufi et al. 2018)
DoAr 25	$-0.02^{+0.04}_{-0.19}$	$-8.3^{+0.5}_{-0.5}$	5.6	(Huang et al. 2018)
DoAr 33	$0.04^{+0.05}_{-0.17}$		2.5	(Huang et al. 2018)
Elias 20	$-0.32^{+0.12}_{-0.07}$	$-6.9^{+0.5}_{-0.5}$		(Huang et al. 2018)
Elias 24	$-0.11^{+0.16}_{-0.08}$	$-6.4^{+0.5}_{-0.5}$		(Huang et al. 2018)
Elias 27	$-0.31^{+0.15}_{-0.11}$	$-7.2^{+0.5}_{-0.5}$		(Huang et al. 2018)
GW Lup	$-0.34^{+0.10}_{-0.17}$	$-9.0^{+0.4}_{-0.4}$	$11.5^{+1.7}_{-1.7}$	(Huang et al. 2018; Garufi et al. 2018)
HD 142666	$0.20^{+0.04}_{-0.01}$	-8.4	15.7	(Huang et al. 2018; Garufi et al. 2018)
HD 163296	$0.31^{+0.05}_{-0.03}$	$-7.4^{+0.3}_{-0.3}$	21.8	(Huang et al. 2018; Garufi et al. 2018)
IM Lup	$-0.05^{+0.09}_{-0.13}$	$-7.9^{+0.4}_{-0.4}$	$3.4^{+1.1}_{-1.1}$	(Huang et al. 2018; Garufi et al. 2018)
MY Lup	0.07	-8.0	$3.3^{+0.9}_{-0.9}$	(Manara et al. 2023; Garufi et al. 2018)
RU Lup	$-0.20^{+0.12}_{-0.11}$	$-7.1^{+0.3}_{-0.3}$	$42.3^{+4.3}_{-4.3}$	(Huang et al. 2018)
SR4	$-0.17^{+0.11}_{-0.14}$	$-6.9^{+0.5}_{-0.5}$	11.6	(Huang et al. 2018)
Sz 114	$-0.76^{+0.08}_{-0.07}$	$-9.1^{+0.3}_{-0.3}$		(Huang et al. 2018)
Sz 129	$-0.08^{+0.03}_{-0.15}$	$-8.3^{+0.3}_{-0.3}$	14.1	(Huang et al. 2018)
WaOph 6	$-0.17^{+0.17}_{-0.09}$	$-6.6^{+0.5}_{-0.5}$	3.0	(Huang et al. 2018)
WSB52	$-0.32^{+0.13}_{-0.17}$	$-7.6^{+0.5}_{-0.5}$		(Huang et al. 2018)
CS Cha	$0.14^{+0.06}_{-0.06}$	-7.9	$2.2^{+0.6}_{-0.6}$	(Parker et al. 2022; Espaillat et al. 2007; Garufi et al. 2018)
Haro 6-13	-0.04	-10.9		(Long et al. 2019; Lin et al. 2023)
AB Aur	$0.36^{+0.04}_{-0.04}$	$-5.6^{+0.11}_{-0.11}$	$27.1^{+2.9}_{-2.9}$	(Garufi et al. 2018; Costigan et al. 2014)
HD 142527	$0.27^{+0.05}_{-0.05}$	$5.7^{+0.22}_{-0.22}$	$34.2^{+3.3}_{-3.3}$	(Parker et al. 2022; Mendigutía et al. 2014; Garufi et al. 2018)
IRS 48	$0.34^{+0.02}_{-0.02}$	-8.5	$2.5^{+11.1}_{-11.1}$	(Garufi et al. 2018; Follette et al. 2015)

Notes. Columns are defined as follows: (1) Source name, (2) Stellar mass, (3) Mass accretion rate, (4) NIR excess (5) References. Values for exoALMA sources are listed in Curone et al. (2025) Table D1. Values for the NIR excess without errors were computed using the procedure outlined in Sect. 5.1. Missing values were not possible to compute or not reported on the literature.